

Digital Topological Analysis of In Vivo Magnetic Resonance Microimages of Trabecular Bone Reveals Structural Implications of Osteoporosis

FELIX W. WEHRLI,¹ BRYON R. GOMBERG,¹ PUNAM K. SAHA,¹ HEE KWON SONG,¹
SCOTT N. HWANG,¹ and PETER J. SNYDER²

ABSTRACT

Osteoporosis is a disease characterized by bone volume loss and architectural deterioration. The majority of work aimed at evaluating the structural implications of the disease has been performed based on stereologic analysis of histomorphometric sections. Only recently noninvasive imaging methods have emerged that provide sufficient resolution to resolve individual trabeculae. In this article, we apply digital topological analysis (DTA) to magnetic resonance microimages (μ -MRI) of the radius obtained at $137 \times 137 \times 350 \mu\text{m}^3$ voxel size in a cohort of 79 women of widely varying bone mineral density (BMD) and vertebral deformity status. DTA is a new method that allows unambiguous determination of the three-dimensional (3D) topology of each voxel in a trabecular bone network. The analysis involves generation of a bone volume fraction map, which is subjected to subvoxel processing to alleviate partial volume blurring, followed by thresholding and skeletonization. The skeletonized images contain only surfaces, profiles, curves, and their mutual junctions as the remnants of trabecular plates and rods after skeletonization. DTA parameters were compared with integral BMD in the lumbar spine and femur as well as MR-derived bone volume fraction (BV/TV). Vertebral deformities were determined based on sagittal MRIs of the spine with a semiautomatic method and the number of deformities counted after threshold setting. DTA structural indices were found the strongest discriminators of subjects with deformities from those without deformities. Subjects with deformities ($n = 29$) had lower topological surface (SURF) density ($p < 0.0005$) and surface-to-curve ratio (SCR; a measure of the ratio of platelike to rodlike trabeculae; $p < 0.0005$) than those without. Profile interior (PI) density, a measure of intact trabecular rods, was also lower in the deformity group ($p < 0.0001$). These data provide the first in vivo evidence for the structural implications inherent in postmenopausal osteoporosis accompanying bone loss, that is, the conversion of trabecular plates to rods and disruption of rods due to repeated osteoclastic resorption. (J Bone Miner Res 2001;16:1520–1531)

Key words: trabecular bone, structure, topological analysis, magnetic resonance imaging, vertebral deformities

INTRODUCTION

IN A consensus conference on diagnosis, prophylaxis, and treatment of osteoporosis at the National Institutes of Health (NIH) osteoporosis was defined as a “disease char-

acterized by low bone mass and microarchitectural deterioration of bone tissue, leading to enhanced bone fragility and increased risk of fracture.”⁽¹⁾ Although the extent of trabecular architecture as an independent contributor to fracture resistance is still debated, there is growing evidence

¹Department of Radiology, University of Pennsylvania Medical Center, Philadelphia, Pennsylvania, USA.

²Department of Medicine, University of Pennsylvania Medical Center, Philadelphia, Pennsylvania, USA.

that bone volume fraction (BV/TV) or bone mineral density (BMD) incompletely characterizes trabecular bone strength.

The significance of the spatial arrangement of a material of given apparent density is fundamental to structural engineering and there is no reason why biomaterials should behave differently. In models of trabecular bone, Jensen et al.⁽²⁾ showed that the apparent stiffness can vary by a factor of 5–10 from perfect cubic lattice to maximum irregularity although trabecular bone volume remains almost constant.

The independent role of architecture in conferring strength to the trabecular network is supported by a large number of experimental studies.^(3–6) Generally, it is agreed that 50–60% of the bone's mechanical competence can be explained by variations in the apparent density (bone mass/tissue volume). The clinical evidence for an independent contribution from trabecular architecture is equally compelling. At least three studies involving histomorphometry in patients with and without vertebral fractures, matched for gender and BMD, found the two groups of subjects to differ in histomorphometric indices.^(7–9)

The invasive nature of bone biopsy-based histomorphometry has so far prevented its widespread use in clinical medicine involving screening of patients at risk of developing osteoporosis. Recently, image-based noninvasive methods based on either peripheral computed tomography (pQCT)^(10–12) or in vivo magnetic resonance microimages (μ -MRI)^(13–17) have emerged as modalities for performing in vivo histomorphometry. MR images hydrogen of the major bone marrow constituents (water and triolein in hematopoietic and fatty marrow, respectively), providing high contrast with the trabeculae, which by virtue of the bone's low mobile hydrogen concentration, appear with background intensity. However, unlike histomorphometry, the achievable image voxel size (a figure of merit for resolution) is not sufficient to fully resolve the trabeculae, causing partial volume blurring due to fractional occupancy of both bone and bone marrow in a significant number of the voxels. Therefore, more sophisticated image analysis methods are needed or, alternatively, instead of true histomorphometric quantities, "apparent" structural parameters derived.

The authors' laboratory has, during the past several years, been devoted to the development of new μ -MRI methods for the acquisition,^(18,19) processing, and analysis of in vivo trabecular bone images.^(17,20–22) In this work we have applied digital topological analysis (DTA) to quantify the architecture of the trabecular bone network in the distal radius of women of widely varying bone density using three-dimensional (3D) μ -MRI and compared the findings with dual-energy X-ray absorptiometry (DXA) BMD. Specifically, we tested the following hypotheses: (i) structural indices in the distal radius, although associated with BMD in the proximal femur and spine, provide additional information not available from bone densitometry and (ii) the distal radius is an appropriate surrogate site for assessing vertebral deformity status.

Topological parameters for a small subset of the patients have been reported previously in an article describing the basic methodology.⁽²²⁾

MATERIALS AND METHODS

Patients

We studied 94 women, of whom 79 were included in the analysis (65 white, 13 black, and 1 Asian; mean age, 54.8 ± 13.0 years; range, 28–76 years). One-third of the women were recruited through newspaper advertisements and medical referrals. The remainder, in roughly equal parts, was recruited from an existing pool of subjects who participated in previous studies, as well as employees at the Medical School of the University of Pennsylvania. Reasons for exclusion from analysis were: wrist size exceeding the maximum allowed by the custom-designed MR wrist coil (7 subjects), low image quality (1 subject), claustrophobia (1 subject); wrist fracture (1 subject), and incomplete data (1 subject).

MRI

μ -MRI was performed in the ultradistal radius of the right hand on a Signa 1.5 T commercial MR scanner with a custom-designed transmit-receive birdcage coil (General Electric, Milwaukee, WI, USA).⁽¹⁷⁾ Subjects were imaged supine with their arms parallel to the body axis. To minimize involuntary subject motion the forearm was immobilized with a fixation device (VacFix; Soule Medical Systems, Inc., Tampa, FL, USA). For the purpose of mapping trabecular architecture, two image series were performed.⁽¹⁷⁾ The first series was a coronal spin-echo localizer scan to prescribe the high-resolution transaxial images of the second image series. For the prescription of the second series, an imaging slab comprising 32 contiguous 350- μ m-thick sections was selected with its distal boundary coincident with the medial cortical end plate, based on the localizer image showing the distal most portion of the radial styloid process. Scan parameters were as follows: image matrix, $512 \times 256 \times 32$; field of view (FOV), $7 \text{ cm} \times 3.5 \text{ cm}$, corresponding to a voxel size of $137 \times 137 \times 350 \mu\text{m}^3$. Radiofrequency (RF) pulse repetition time (TR) and echo time (TE) were 80 ms and 11 ms, respectively, RF pulse flip angle was 140° . Scan time was 1 minute for the localizer scan of the first image series and 11 minutes for the second series, providing the images from which architectural parameters were derived. The pulse sequence was developed in our laboratory as a derivative of the original fast large-angle spin-echo (FLASE) pulse sequence⁽¹⁸⁾ by adding motion-sensing navigator echoes as a means to correct for translational motion of the forearm.⁽¹⁹⁾ A typical low-resolution localizer image of the distal forearm, along with 1 of the 32 axial high-resolution images, is shown in Fig. 1. Finally, sagittal fast spin-echo images were acquired so as to cover the lumbar and thoracic spine using the following scan parameters: image matrix, 512×256 ; FOV, $40 \text{ cm} \times 40 \text{ cm}$; TR, 2000 ms; TE, 60 ms; scan time, 2 minutes.

Image processing

All processing of the images was performed off-line, either in Interactive Data Language (IDL; RSI Inc., Boulder, CO, USA) or using custom-designed routines programmed in "C." The first step involved the navigator motion correc-



FIG. 1. (A) Coronal localizer MRIs of the distal forearm and (B) one of the 28 high-resolution images showing metaphyseal trabecular structure in the radius and ulna. The image voxel size of the high-resolution image in panel B is $137 \times 137 \times 350 \mu\text{m}^3$.

tion, which consisted of applying a phase correction to the k-space data based on the positional displacement measured by the navigator in x and y direction (i.e., in the plane perpendicular to the radial axis) as described by Song et al.⁽¹⁹⁾ The k-space data corrected in this manner were then filtered and Fourier transformed in the usual manner to yield 28 contiguous axial images of the distal epiphysis. The volume of interest (VOI) for subsequent processing and analysis was selected manually on each of the 28 slices by tracing a line approximately 1 mm from the endocortical boundary. Thus, the VOI consisted of the entire cross-section in order to prevent errors from inconsistent localization. The second step consisted of the computation of BV/TV maps,⁽²⁰⁾ that is, images in which the pixel intensity represents the fraction of the imaging voxel occupied by bone. This approach has been shown advantageous because it does not require applying an intensity threshold to assign each voxel to either bone or bone marrow because at in vivo resolution partial volume mixing occurs so that virtually every bone-containing voxel is partially occupied by marrow as well. BV/TV was calculated from the BV/TV maps as the average from all voxels within the VOI. Finally, the images were subjected to subvoxel processing,⁽²³⁾ a method that alleviates the blurring incurred by partial volume averaging due to image voxels occupied by both bone and bone marrow. The principle consists of subdividing imaging voxels and reallocating intensities based on local neighborhood criteria under strict mass conservation. Application of the algorithm resulted in a $70 \times 70 \times 90 \mu\text{m}^3$ voxel size. The subvoxel-processed images have features characteristic of images acquired at higher spatial resolution.

DXA

DXA was performed on a Lunar DPX dual-energy X-ray absorptiometer (Lunar Corp., Madison, WI, USA). Measurements were taken in the lumbar spine and proximal femur using the scanner's standard acquisition and processing software. Lumbar BMD values were collected for vertebrae L1–L4. The proximal femur was evaluated bilaterally and BMD values were ascertained for the total femur, femoral neck, trochanter, and Ward's triangle. BMD T scores were tabulated as calculated based on the manufacturer's reference database.

Measurement of vertebral deformity

There are no internationally agreed on criteria for what constitutes a vertebral fracture based on radiographic ap-

pearance.^(24,25) Here, we therefore refer to “vertebral deformity” as the quantity resulting from a morphometric measurement, as opposed to a “fracture” defined as a deformity exceeding a given threshold of deformity. This is the approach used most commonly in vertebral morphometry.⁽²⁵⁾ Vertebral deformity was determined based on the sagittal MRIs of the spine acquired as part of the MR protocol analogous to prior work^(17,26) and based on the method of Eastell et al.⁽²⁷⁾ To account for scoliosis and sagittal obliquity, the slices exhibiting maximum spinal cord cross-section at the respective vertebral levels were selected manually and interpolated to obtain a midline spinal image. Vertebral shape was quantified by manually selecting the two anterior and posterior “corners” of each vertebra. Subsequently, the program automatically bisected each vertebra using the previously selected corner points and determined the midvertebral inferior and superior margins along this bisecting line. The resulting six points define the anterior, middle, and posterior heights of each vertebra yielding the three measures of deformity: biconcavity, wedge, and compression.

Biconcavity deformity (bicon) was obtained as the reduction in midline height (H_m) relative to the average of the posterior and anterior heights (H_p and H_a , respectively), that is, $\text{bicon} = 1 - H_m / ((H_a + H_p) / 2)$. Wedge deformity (wedge) was expressed as the percent reduction in anterior relative to posterior height, that is, $\text{wedge} = (H_p - H_a) / H_p$. Because the curvature of the spine causes wedge “deformities” even in the absence of pathology, the average wedge deformity for all subjects in this study was computed and used as a baseline from normal wedge deformities at each vertebral level. Biconcavity deformities were adjusted similarly to a baseline value of 11% that was constant for all vertebral levels.

In the analysis of compression deformities (comp) the first step was to take the average height of each vertebra $((H_a + H_p + H_m) / 3)$, which was used for all subsequent compression deformity analyses. Compression deformities were more difficult to assess because of the need for a “normal” height against which the measured height could be referenced. The interpolated average height of the previous and next vertebra did not always work in the case of vertebrae at the edges of the FOV and in situations of multiple consecutive compression deformities. Details of this estimation method will be reported elsewhere.

Once the vertebral deformities were determined, a vertebra was considered fractured if it had any deformity over 15%, as proposed previously.⁽²⁴⁾ In this manner, the number

of fractures (NFX) for each subject was determined. To compensate for the different severity of each type of deformity, a weighting scheme⁽²⁸⁾ was used that set the relative values for bicon, wedge, and comp fractures at 1, 1.5, and 3, respectively, resulting in the weighted NFX (WNFX). Finally, a spinal deformity index (SDI) was computed by summing the weighted deformities over most of the T spine (typically from T4 or T5) and the entire L spine for each subject. Thereafter, the study population was divided into two groups, a “fracture” and a “nonfracture” group, by setting thresholds for WNFX ($WNFX \geq 1 = \text{fracture}$) and for SDI ($SDI \geq 262 = \text{fracture}$). Both classification schemes were subsequently evaluated with respect to the discriminating ability of the MR and DXA parameters.

Topological analysis of trabecular bone images

Recently, we have reported a new method for characterizing the topology of the trabecular bone network by means of what is referred to as DTA.^(21,22) The method is based on algorithms that allow unambiguous assignment of the topological class to each image voxel by inspecting each bone voxel's $3 \times 3 \times 3$ neighborhood. The process begins with converting the 3D image to a skeletonized surface representation after the images have been binarized. The skeletonization process ensures that the resulting image consists of 1D and 2D structures only (i.e., surfaces and curves), which is essential for the algorithm to work. We shall refer to plate and rodlike elements of the trabecular structure as “plates” and “rods” as opposed to their topological counterparts, which are surfaces and curves to which the former are converted by skeletonization. The methodology for parameter extraction has been described previously and thus only a brief summary is given. The topological classes of an idealized trabecular network are illustrated in Fig. 2. Isolated voxels typically are artifactual because topologically the network consists of a single object. Profiles comprise any surface edge (SE)-type voxel with no neighboring surface (S), surface-curve (SC), or surface-surface (SS) junction-type voxels. The topological classes and their abbreviations, along with derived parameters, are summarized in Table 1. Derived parameters that were found useful are the surface-to-curve ratio (SCR) and the erosion index (EI). The latter represents a quantity that is sensitive to the network erosion from osteoclastic action as it is predominant during aging and osteoporosis and which entails conversion of plates to rods.⁽²⁹⁾ Consequently, the EI was defined as the ratio of all topological parameters expected to increase during the erosion process (C [curve] type, curve edge [CE] type, SE type, profile edge [PE] type, and curve-curve [CC] type) compared with those that are expected to decrease (S type and SS type). The various steps involving acquisition, processing, and analysis of the images are illustrated in Fig. 3.

Of particular concern was whether network topology was preserved in images acquired at the much lower resolution regime of in vivo μ -MRI, although the apparent resolution of the images was enhanced by subvoxel processing (as shown previously). This question was addressed in prior work in the form of synthetic images consisting of inter-

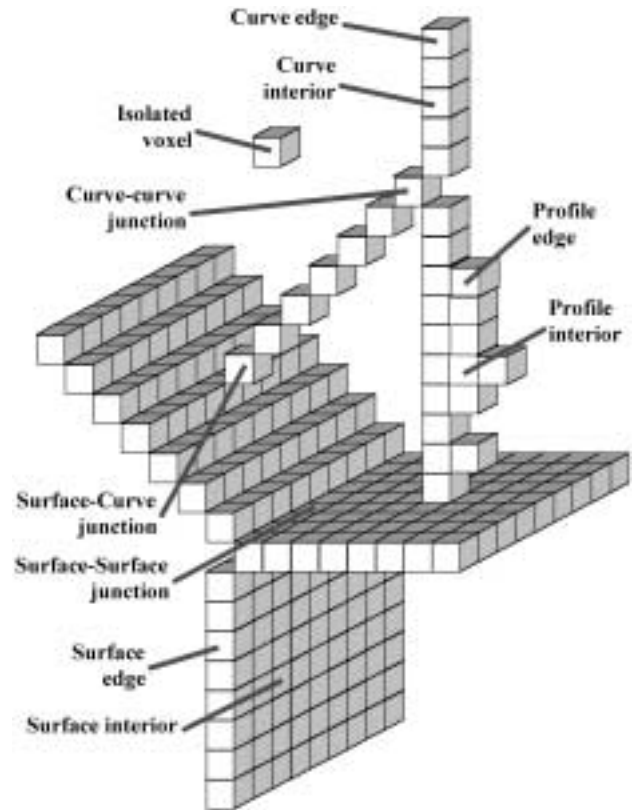


FIG. 2. Topological classes of image voxels in idealized skeletonized network consisting of surfaces and curves. Abbreviations used for topological classes are given in Table 1.

secting plates and rods in which the topology is known a priori.⁽²²⁾ The results of this evaluation for the plate model showed that for structural resolutions up to 0.6 (plate thickness/voxel size) the accuracy was 98% or better. In this work we further validated DTA with a set of in vitro data from distal radius specimens from 8 donors obtained as part of two earlier studies.^(6,22) “Gold standard” images were created from each of the $128 \times 128 \times 128$ voxel 3D arrays ($78\text{-}\mu\text{m}$ voxel size) of μ -MRI images by subvoxel processing to $39 \times 39 \times 39 \mu\text{m}^3$ voxel size. These images were subsequently resampled to yield images of $156 \mu\text{m}$ resolution, similar to the ones obtained in vivo. The resampled low-resolution images were then processed analogous to the in vivo images by subjecting them to subvoxel processing and DTA parameters were determined. The degree of correlation of DTA parameters obtained at the gold standard $39\text{-}\mu\text{m}$ resolution with those derived from the images simulated under in vivo conditions is a measure of the sensitivity of DTA to structural resolution, that is, the resolution relative to the characteristic size of the structural elements examined.

In Fig. 4 selected topological parameters, derived from images at in vivo resolution, are compared with those obtained at gold standard $39\text{-}\mu\text{m}$ resolution. It is noted that voxel counts for both SE- and profile-interior (PI)-type voxels derived from images in the two very different resolution regimes are highly correlated, although the absolute voxel counts computed from

TABLE 1. DEFINITION OF TOPOLOGICAL PARAMETERS

	<i>Variable description</i>	<i>Notes/formula</i>
DENS	Topological skeleton density	Fraction of all bone voxels in the skeleton
CE	Curve edge voxel density	
SE	Surface edge voxel density	
C	Curve interior voxel density	
S	Surface interior voxel density	
CC	Curve-curve junction density	
SC	Surface-curve junction density	
SS	Surface-surface junction density	
PE	Profile edge voxel density	
PI	Profile interior voxel density	
SURF	All surface voxel density	$S + SE + SS$
CURV	All curve voxel density	$C + CC + PE/2$
JUNC	All junction voxel density	$SC + SS + CC$
SCR	Surface to curve ratio	$SURF/CURV$
EI	Topological erosion index: ratio of parameters expected to increase divided by those expected to decrease upon skeleton erosion	$(C + CE + SE + PE + CC)/(S + SS)$

All parameters are dimensionless, representing densities, defined as the number of image voxels of the represented type, divided by all voxels in the VOI.

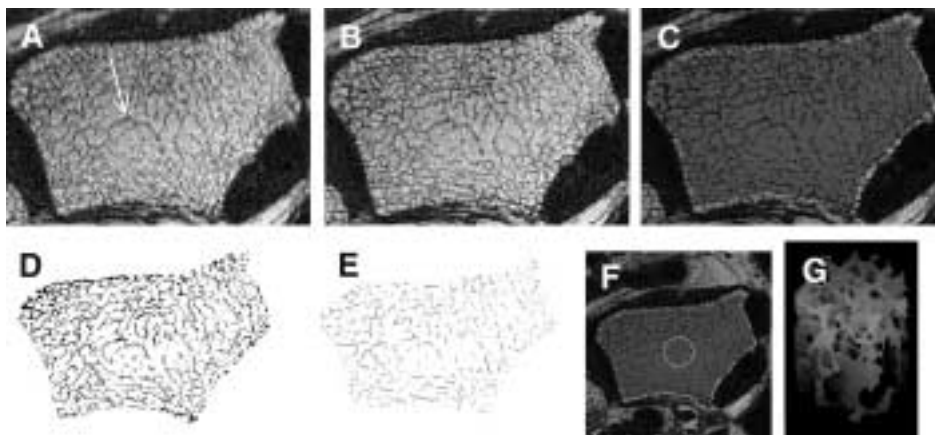


FIG. 3. Stages involving acquisition, processing, and analyses of the trabecular bone images. (A) Raw data; (B) motion corrected; (C) BV/TV map following histogram deconvolution; (D) subvoxel processed; (E) map after topological classification (surfaces in black, curves in gray); (F) localization of virtual core; (G) 3D shaded surface projection of virtual core. Notice that the arch-shaped structure (arrow in panel A) is visible in all images.

the lower-resolution images are lower, causing the slopes to differ from unity. However, most importantly, the relative numbers of voxels of a particular topological type are largely preserved at in vivo resolutions. The correlations for other parameters comparing the two resolution regimes varied but were similar in magnitude.

Statistical analyses

The following analyses were performed. First, a comparison was shown of BV/TV and structural parameter from DTA with DXA BMD at all sites measured, that is, the lumbar spine and the three femoral sites using linear correlation. Second, to evaluate whether any of the parameters measured could distinguish the fracture from the nonfracture group, two-sided *t*-tests were performed. Fracture status was defined with the two algorithms described previously. Parameters examined comprised 15 DTA parameters and BV/TV measured in the distal radius, as well as DXA BMD

measured at three femoral sites and the lumbar spine, the latter as the average of L2–L4.

RESULTS

Relationship between structure and BV/TV and BMD

Table 2 lists the correlation coefficients for associations between MR-derived structural parameters measured in the distal radius and DXA BMD at the spine and femoral sites. The data indicate that radial BV/TV is associated with both vertebral and femoral BMD sites. Most correlations are highly significant and positive. Noteworthy exceptions in terms of the sign of the correlation are those comprising parameters that are expected to increase with decreasing bone density (e.g., EI, CE, and CC junction density), which all are related to the conversion of plates to rods in response to bone volume loss. One of the strongest associations found is between the topological surface voxel density (parameter

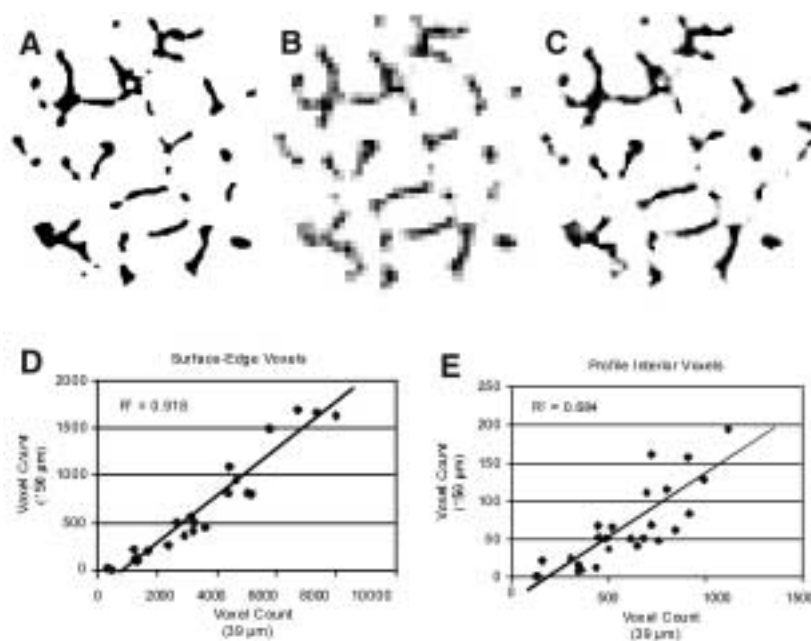


FIG. 4. Resolution dependence of topological parameters. (A) Sample “gold standard” BV/TV map (39- μm isotropic voxels), derived from μ -MRIs from specimens of the distal radius, harvested postmortem⁽⁶⁾; (B) BV/TV map from the same VOI after resampling the entire 3D data set to yield $156 \times 156 \times 156 \mu\text{m}^3$ voxel size, causing partial volume blurring; (C) result of subvoxel processing the image data in panel B; (D) SE count derived from low-resolution ($156 \times 156 \times 156 \mu\text{m}^3$) images versus that obtained from gold standard ($39 \times 39 \times 39 \mu\text{m}^3$) images; (E) same as panel C but for curve voxel counts.

TABLE 2. CORRELATION COEFFICIENTS FOR CORRELATIONS BETWEEN BV/TV OR DTA STRUCTURAL PARAMETERS AND DXA BMD T SCORES ($n = 79$)

Parameter	T_{L2-L4}	T_{NECK}	T_{TROCR}	T_{WARD}	p
BV/TV	0.58	0.59	0.64	0.60	<0.0001
DENS	0.58	0.54	0.60	0.54	<0.0001
CE	-0.39	-0.46	-0.52	-0.49	<0.0005
SE	0.63	0.61	0.66	0.62	<0.0001
C	-0.15	-0.16	-0.09	-0.17	NS
S	0.61	0.58	0.59	0.58	<0.0001
CC	-0.37	-0.41	-0.37	-0.42	<0.001
SC	0.55	0.52	0.58	0.51	<0.0001
SS	0.50	0.47	0.52	0.44	<0.0001
PE	0.27	0.28	0.35	0.30	<0.05
PI	0.64	0.65	0.66	0.68	<0.0001
SURF	0.64	0.61	0.63	0.61	<0.0001
CURV	-0.16	-0.19	-0.12	-0.19	NS
JUNC	0.38	0.32	0.40	0.32	<0.005
SCR	0.58	0.56	0.57	0.57	<0.0001
EI	-0.42	-0.43	-0.45	-0.42	<0.0001

For definition of parameters see Table 1 and Fig. 2.

expressing the “plate-likeness” of the trabeculae) and DXA BMD in the lumbar vertebrae ($r = 0.64$; Table 2). Nevertheless, the magnitudes of the correlations suggest that a large fraction of the variance in structure is unexplained by changes in integral bone density in the spine and femur.

Association between trabecular BV/TV and DTA structural parameters

Most of the trabecular structural parameters obtained by DTA at the distal radius site are significantly correlated with BV/TV (Table 3), though the strength of the

correlations varies. Again, it is interesting to note that certain parameters are correlated negatively. These include CE, CC, and EI. Such a behavior is plausible because bone loss leads to disconnection of rods leading to an increase of “free ends”⁽⁸⁾ (topological counterpart is CE) and increased erosion. Figure 5 shows associations between BV/TV and topological surface density (SURF) and EI. Clearly, there is a disproportionately large effect on architecture paralleling a change in bone volume, as manifested by the much larger range in the architectural parameters (e.g., a factor of 10 for SURF for a factor of 2 change in BV/TV).

TABLE 3. ASSOCIATION BETWEEN DTA STRUCTURAL PARAMETERS IN THE DISTAL RADIUS AND TRABECULAR BV/TV

DTA parameter	r	p
DENS	0.89	<0.0001
CE	-0.74	<0.0001
SE	0.92	<0.0001
C	-0.01	NS
S	0.82	<0.0001
CC	-0.42	<0.0001
SC	0.91	<0.0001
SS	0.85	<0.0001
PE	0.53	<0.0001
PI	0.86	<0.0001
SURF	0.89	<0.0001
CURV	-0.06	NS
JUNC	0.72	<0.0001
SCR	0.78	<0.0001
EI	-0.71	<0.0001

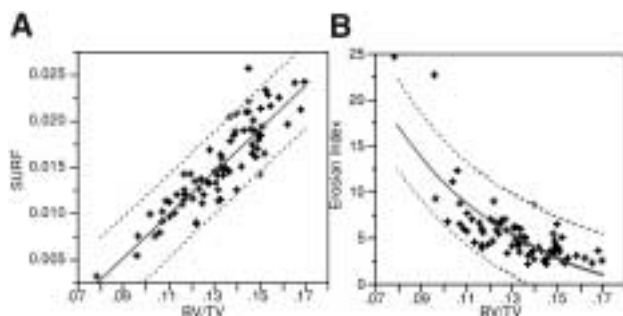


FIG. 5. Trabecular BV/TV versus DTA structural parameters. (A) SURF; (B) EI. Correlation coefficients for both regressions were 0.89. In panel B the model used was an inverse relationship (hyperbola) between the two parameters compared.

Associations between vertebral deformity status and BMD and structure

The two classification schemes of vertebral deformity defined in the Materials and Methods section (based on WNFx and SDI), after thresholding, yielded 28 and 29 subjects with fractures, respectively, from the pool of 79 patients. In Fig. 6 characteristic images from subjects with normal trabecular network topology and vertebral morphology are compared with the image data from patients with abnormal trabecular architecture and vertebral deformities. Means, SEs, and significance for both DTA parameters and DXA BMD are reported in Tables 4 and 5.

We first notice that the discriminating ability of the structural and BMD parameters differ substantially for the two measures of vertebral deformity. When WNFx was used as a criterion for the presence of vertebral deformity, DXA BMD measured at any one site was unable to distinguish fracture from nonfracture, although the trends suggest the expected lower T scores to be associated with the fracture group (Table 4). By contrast, the trabecular volume fraction

in the distal radius (BV/TV) was lower in the fracture group ($12.7 \pm 0.3\%$ vs. $13.8 \pm 0.2\%$; $p = 0.01$). Further, 8 of the 15 topological parameters were significantly different in the fracture group, with the EI ($p = 0.006$) and the SCR ($p = 0.01$) being the strongest discriminators.

Determination of the vertebral fractures by summing all vertebral deformities and setting a threshold on the resulting deformity index, which is a continuous variable (see Materials and Methods section for details), yielded similar results but the associations were considerably stronger (Table 5). All BMD sites were significantly lower in the fracture group. Again, μ -MRI-derived BV/TV was a stronger discriminator of the two groups than L2–L4 DXA BMD ($p = 0.002$ vs. 0.01 , respectively) but the femoral sites were similar in significance. Ten of the 15 DTA parameters were significantly different in the fracture group. Particularly discriminating were structural parameters that are measures of plate density (S, SE, SURF, and SCR), which were all lower in the fracture group ($p < 0.001$) supporting the view that osteoporotic bone loss is associated with loss of plate-like bone. Scatter plots comparing BMD and SCR as discriminators of the two groups are shown in Fig. 7. By far, the strongest discriminator was PI, which was considerably lower in the fracture group ($p < 0.0001$), suggesting bone loss as causing disruption of trabecular struts. This interpretation is supported further by the higher density of CEs in the fracture group, consistent with bone loss leading to generation of “free ends” or termini.⁽⁸⁾

DISCUSSION

Digital topology of trabecular bone networks and relationship to BV/TV and BMD

The significance of the topological properties of trabecular bone networks has been recognized early. Feldkamp et al.⁽³⁰⁾ reasoned that connectivity is impossible to derive from images of 2D sections. They expressed connectivity in terms of the Euler number N as connectivity = $1 - N$. Lane et al.⁽³¹⁾ showed that ovariectomized rats, when treated with estrogen, could restore their preovariectomy bone volume but not the lost connections, thus showing the disparate behavior of BV/TV and network topology. Pothuaud et al.⁽³²⁾ extended the classical approach toward establishing topological quantities such as the Euler-Poincaré number, counts of branches, and termini based on skeleton graphs. These are derived by a thinning algorithm that converts the trabecular structure to a network of curves, eliminating plates altogether. Classical topology in terms of the Euler number ignores the existence of plates and rods and may fail to detect the effect of osteoporotic erosion as has been pointed out by Kinney and Ladd.⁽³³⁾ Consider, for example, a rodlike loop of a trabecula attached to a plate. Clearly, breaking the loop would decrease connectivity by one while fenestration of the plate would increase connectivity. Thus, disrupting the loop simultaneously with a single perforation of the trabecular plate would have no net effect on connectivity! DTA, in which each voxel's topology is identified and classified, is not subject to such ambiguities.

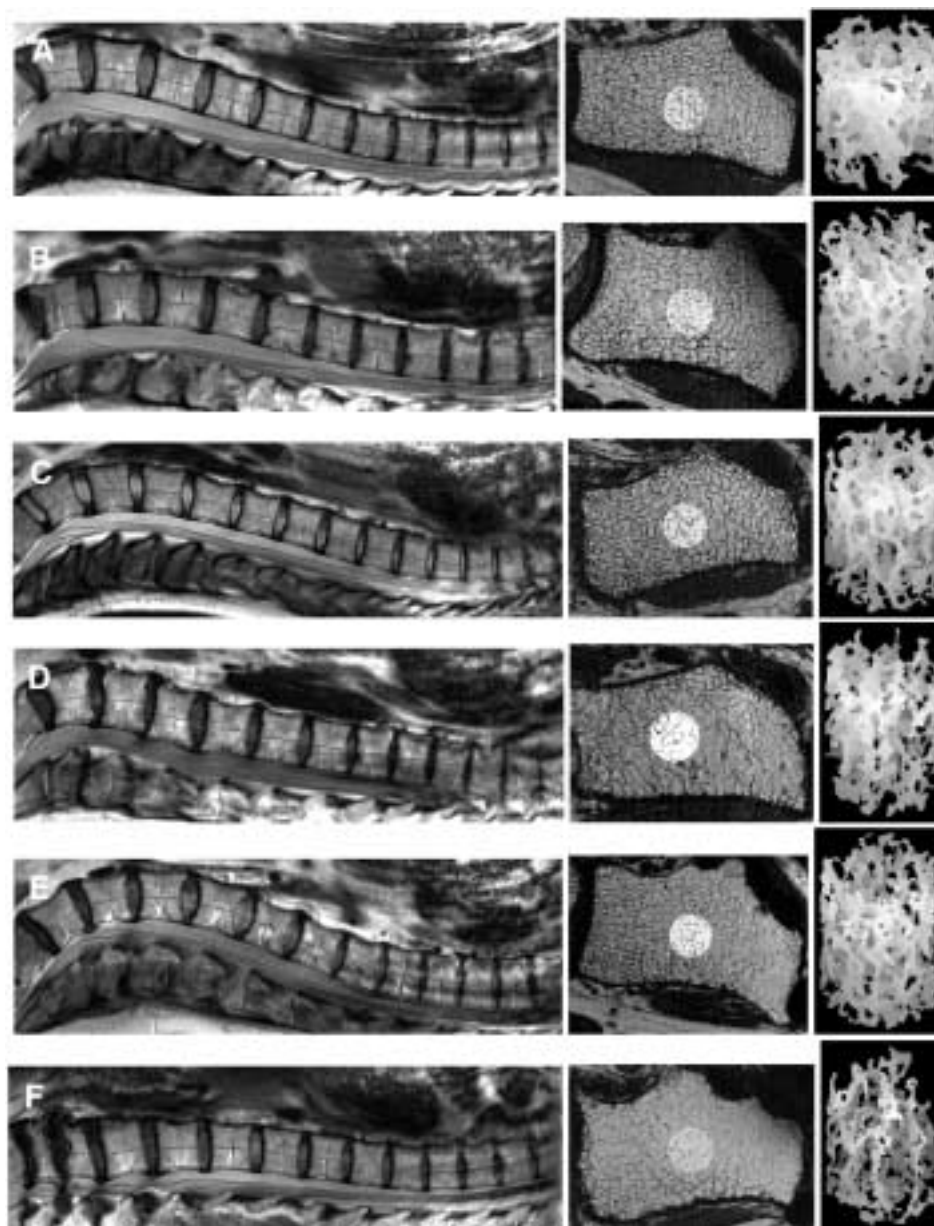


FIG. 6. Spine, cross-sectional radius, and virtual core 3D surface projections from ROI indicated (left, center, and right) for (A–C) three subjects without spinal deformities and (D–F) three with deformities. DXA-BMD (L2–L4) indicated that subjects in panels A and C were normal, in panels D–F were osteopenic, and in panel B was osteoporotic. Patients with vertebral fractures had low values of the SCR (0.5, 0.4, and 0.2) and high EI (6.9, 8.7, and 24.5) unlike their normal peers (1.3, 0.7, and 1.4 and 2.1, 4.4, and 2.1 for SCR and EI, respectively).

Various approaches have been described to distinguish rodlike from platelike architectures. Hahn et al.⁽³⁴⁾ found the proportion of trabecular plates to rods to be reflected by the ratio of concave to convex surfaces, expressed in terms of the “trabecular bone pattern factor.” An elegant algorithm making use of the change in surface area for a differential change in radial expansion led to the definition of a parameter denoted “structure-model index” (SMI).⁽³⁵⁾ This metric was subsequently applied to the quantitative characterization of 3D μ -CT trabecular bone images from multiple anatomic locations known predominantly to be platelike (SMI 0–1) or rod-like (SMI 2–3).⁽³⁶⁾ In prior work, Gomberg et al.⁽²²⁾ showed, in high-resolution μ -MR images of the distal radius, variations in topological SC by over one order of magnitude, in good qualitative agreement with the visual appearance of the different morphologies.

It is, of course, well known that structural parameters scale with BMD (and thus BV/TV) because any loss in bone volume typically is accompanied by topological changes. Such an etiology is well established in age-related bone loss or bone loss due to estrogen deficiency (as opposed to steroid-induced osteoporosis in which homogeneous thinning may occur without significant architectural changes).⁽³⁷⁾ Therefore, in this light, it is not surprising that the topological parameters parallel, to varying extent, BV/TV at the radius but also DXA BMD at both femur and spine. (Tables 2 and 3). However, the correlation coefficients indicate that typically 65% ($r^2 = 0.35$) or more of the variances in structure are unexplained by changes in BMD or BV/TV. The relationships are stronger between BV/TV and DTA parameters because they relate to comparisons at the same site. The strongest positive associations are found for correlations involving surface voxel densi-

TABLE 4. COMPARISON OF DXA BMD T SCORES AND ARCHITECTURAL PARAMETERS MEASURED IN THE RADIUS BY DTA IN PATIENTS WITH AND WITHOUT VERTEBRAL FRACTURES ($n = 28$ AND $n = 51$, RESPECTIVELY), BASED ON THE WNFx WITH $WNFX \geq 1$ AS A FRACTURE CLASSIFICATION CRITERION

Parameter	Fracture	Nonfracture	Significance (p)
BMD L2-L4	-1.17 ± 0.33	-0.63 ± 0.25	NS
BMD femoral neck	-1.53 ± 0.24	-1.02 ± 0.17	NS
BMD Ward's trochanter	-1.69 ± 0.28	-1.06 ± 0.20	NS
BMD trochanter	-0.94 ± 0.22	-0.70 ± 0.17	NS
BV/TV	12.7 ± 0.3	13.8 ± 0.2	0.01
DENS	39.8 ± 0.98	41.9 ± 0.72	NS
CE	1.11 ± 0.03	1.03 ± 0.02	0.03
SE	7.19 ± 0.32	8.05 ± 0.24	0.04
C	16.53 ± 0.35	15.98 ± 0.26	NS
S	6.01 ± 0.57	7.75 ± 0.42	0.02
CC	1.74 ± 0.05	1.59 ± 0.04	0.03
SC	2.48 ± 0.09	2.66 ± 0.07	NS
SS	0.21 ± 0.02	0.23 ± 0.01	NS
PE	3.94 ± 0.09	4.04 ± 0.07	NS
PI	3.51 ± 0.02	4.08 ± 0.01	0.02
SURF	13.46 ± 0.87	16.03 ± 0.65	0.02
CURV	21.34 ± 0.42	20.61 ± 0.34	NS
JUNC	4.43 ± 0.11	4.49 ± 0.08	NS
SCR	0.638 ± 0.050	0.797 ± 0.037	0.01
EI	6.75 ± 0.65	4.47 ± 0.48	0.006

Reported are means \pm SE using one-way ANOVA. For definition of structural parameters, see Fig. 2 and Table 1. Topological densities are listed as actual $\times 10^3$. BV/TV is in percent.

ties (SE, S, SC, and SS; $r = 0.82$ – 0.92) suggesting that decreases in bone volume occur at the expense of plates, that is, supporting the notion of fenestration due to inhomogeneous erosion.⁽³¹⁾ Among the three significant negative correlations are those involving CE and EI (EI; $r = -0.74$ and -0.71 , respectively). The increase in CE with decreasing BV/TV is consistent with the disruption of trabecular struts and the creation of free ends.⁽⁸⁾ The associations between DTA parameters and BMD at the femoral and vertebral sites are analogous in sign and relative magnitude but generally are weaker than the corresponding intrasite correlations (Table 3). This finding is plausible considering that DXA BMD does not represent trabecular volume density and that BMD at these locations may vary in a site-specific manner.

Of particular interest is the range across which a parameter changes because this quantity indicates a particular parameter's relative sensitivity. BMD T scores in the patients studied vary between about -4 and $+4$ (or from about 0.7 g/cm² to about 1.6 g/cm²). Likewise, radial BV/TV was found to cover a range from 8% to about 17%, comparable in magnitude to BMD (i.e., $\sim 100\%$). By contrast, the topological surface voxel density and EI vary over a range of a factor of 6 and 10, respectively (Fig. 5) in the study population. Therefore, the data suggest that structural changes in response to a change in BV/TV or BMD are magnified greatly. If measurable with sufficient precision, these parameters should therefore prove useful to detect small changes in response to treatment and to follow progression or regression of disease.

Trabecular network architecture as a predictor of vertebral deformity status

The results suggest that the structural changes shown in the distal radius are likely to be paralleled by similar changes at the site of deformity and lend further support to the potential of architecture as predictors of osteoporotic vertebral deformities.^(7–9,15,17) Kleerekoper et al.⁽⁷⁾ first showed that women with osteoporosis and vertebral compression deformities had a significantly lower mean trabecular plate density than women without deformities, matched for age and BMD. Similarly, Recker⁽⁸⁾ showed that a subset of patients with vertebral crush fractures, matched to an equal number of controls for trabecular bone volume, had considerably decreased trabecular plate density and increased marrow star volume.⁽³⁸⁾ Very recently, Legrand et al.,⁽⁹⁾ who studied 108 men with osteoporosis of whom 62 had at least one vertebral fracture, showed that the patients with fractures did not differ in age, BMD of the spine, or hip from those without fractures. However, trabecular number was lower and trabecular separation was greater in the fracture group. Other distinguishing histomorphometric parameters were found to relate to network connectivity.

All of the foregoing work is based on histomorphometry of transiliac bone biopsy specimens. In contrast, attempts to discriminate patients with osteoporotic fractures based on noninvasive imaging of architecture have been relatively few.^(15,17,39,40) In a pilot study involving 20 women of varying degree of osteoporosis, Wehrli et al.⁽¹⁷⁾ found that neither BMD nor any of the structural parameters individ-

TABLE 5. COMPARISON OF DXA BMD T SCORES AND DTA ARCHITECTURAL PARAMETERS MEASURED IN THE RADIUS IN PATIENTS WITH AND WITHOUT FRACTURES ($n = 29$ AND $n = 50$, RESPECTIVELY), BASED ON THE VERTEBRAL DEFORMITY INDEX (SDI) WITH $SDI \geq 262$ AS A FRACTURE CLASSIFICATION CRITERION

Parameter	Fracture	Non-Fracture	Significance (p)
BMD L2-L4	-1.50 ± 0.24	-0.43 ± 0.32	0.01
BMD femoral neck	-0.90 ± 0.23	-1.72 ± 0.23	0.006
BMD Ward's trochanter	-1.98 ± 0.25	-0.88 ± 0.20	0.001
BMD trochanter	-1.32 ± 0.21	-0.48 ± 0.16	0.002
BV/TV	12.56 ± 0.32	13.83 ± 0.24	0.002
DENS	38.8 ± 0.9	42.6 ± 0.7	0.002
CE	1.12 ± 0.03	1.02 ± 0.02	0.008
SE	6.81 ± 0.30	8.29 ± 0.23	0.0002
C	16.46 ± 0.34	16.00 ± 0.26	NS
S	5.65 ± 0.54	8.02 ± 0.41	0.0008
CC	1.75 ± 0.05	1.58 ± 0.04	0.009
SC	2.37 ± 0.09	2.72 ± 0.07	0.002
SS	0.20 ± 0.02	0.24 ± 0.01	NS
PE	3.89 ± 0.09	4.07 ± 0.07	NS
PI	0.33 ± 0.02	0.42 ± 0.01	<0.0001
SURF	12.66 ± 0.82	16.55 ± 0.62	0.0003
CURV	21.27 ± 0.42	20.64 ± 0.32	NS
JUNC	4.32 ± 0.10	4.55 ± 0.08	NS
SCR	0.602 ± 0.047	0.821 ± 0.036	0.0004
EI	6.94 ± 0.63	4.31 ± 0.48	0.001

See Table 4 for additional detail.

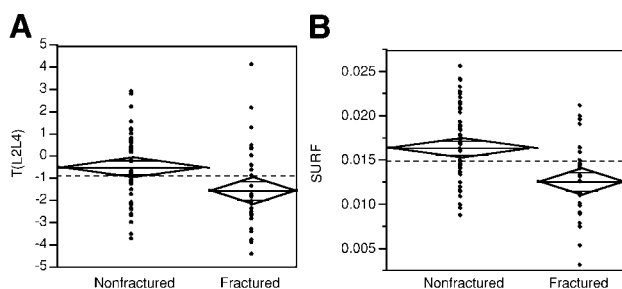


FIG. 7. Scatter plots comparing (A) BMD T scores (average L2-L4) and (B) the topological SCR as discriminators of fracture. The means are different at the (A) $p = 0.01$ and (B) $p = 0.0004$ level.

ually correlated significantly with vertebral deformity fraction, whereas a simple function of two architectural parameters obtained by μ -MRI predicted deformity fraction well ($r = 0.78$; $p = 0.005$). Link et al.⁽¹⁵⁾ reported that MRI-derived texture measures in the calcaneus were able to separate hip fracture from patients without fractures better than hip BMD.

The strengths of the associations clearly depend on the manner in which fractures are defined (Tables 4 and 5). The SDI probably more accurately expresses total deformity load because it represents a sum of all deformities from baseline, no matter how small they are because no threshold is applied. By contrast, the NFX counts only deformities greater than 15% from baseline. Therefore, the current data would suggest that even small deformities, well below the 15% threshold, may be abnormal and may be associated with structural deterioration of the trabecular network.

This work distinguishes itself from its predecessors in that it is the first to show superior associations between vertebral deformity and a number of architectural indices measured in the distal radius. The results also establish the radius as an appropriate surrogate site for probing the architectural changes that are known to accompany bone loss in the vertebrae. Further, the approach of DTA in which each voxel of a digital image is assigned to a unique class is in itself novel and has not been applied previously to trabecular bone networks.

The findings bear the hallmarks of postmenopausal bone loss characterized by conversion of plates to rods from increased deepening of osteoclastic resorption cavities in repeated remodeling cycles, eventually leading to plate perforation.⁽²⁹⁾ Such a sequel would result in a net reduction in all surface voxel densities (S, SE, and SURF) as well as the SCR, which are all substantially lower in the fracture group (all $p < 0.001$; Table 5). Likewise, the osteoclastic erosion process causes disruption of trabecular struts, as it is well established in the bone electron microscopy literature,⁽⁴¹⁾ resulting in increased population of free ends or termini.⁽⁸⁾ There is clear evidence in the data for a greater proportion of free ends in the fracture group. The topological consequences of this process involve an increase of CE voxels in the fracture group ($p = 0.008$) and a consequent decrease in PI voxels ($p < 0.0001$; Table 5). To the best of our knowledge, this is the first in vivo manifestation of the disease-specific conversion of trabecular plates to rods in postmenopausal osteoporosis.

We have shown that trabecular bone structure analysis based on a complete voxel-by-voxel characterization of

network topology provides insight into the architectural changes that occur during the pathogenesis of osteoporosis, that is, the conversion of plates to rods and the disruption of rodlike trabecular elements, hitherto evident only from *ex vivo* bone biopsy. The strong associations between trabecular structure in the distal radius and the extent of vertebral deformities support the hypothesis that impaired integrity of the trabecular network at the distal radius site parallels similar changes in the spine. Further, the range of some of the topological parameters exceeds the changes in terms of bone density or BV/TV by nearly an order of magnitude, suggesting the architectural consequences of bone loss to be significantly amplified.

ACKNOWLEDGMENTS

This work was supported by the NIH (RO1 41443, T32 CA 74781, and RO1 40671).

REFERENCES

- 1993 Consensus Development Conference: Diagnosis, prophylaxis, and treatment of osteoporosis. *Am J Med* **94**:646–650.
- Jensen KS, Mosekilde L, Mosekilde L 1990 A model of vertebral trabecular bone architecture and its mechanical properties. *Bone* **11**:417–423.
- Gordon CL, Webber CE, Nicholson PS 1998 Relation between image-based assessment of distal radius trabecular structure and compressive strength. *Bioengineering* **49**:390–397.
- Oden ZM, Selvitelli DM, Hayes WC, Myers ER 1998 The effect of trabecular structure on DXA-based predictions of bovine bone failure. *Calcif Tissue Int* **63**:67–73.
- Siffert RS, Luo GM, Cowin SC, Kaufman JJ 1996 Dynamic relationships of trabecular bone density, architecture, and strength in a computational model of osteopenia. *Bone* **18**:197–206.
- Hwang SN, Wehrli FW, Williams JL 1997 Probability-based structural parameters from 3D NMR images as predictors of trabecular bone strength. *Med Phys* **24**:1255–1261.
- Kleerekoper M, Villanueva AR, Stanciu J, Sudhaker Rao D, Parfitt AM 1985 The role of three-dimensional trabecular microstructure in the pathogenesis of vertebral compression fractures. *Calcif Tissue Int* **37**:594–597.
- Recker RR 1993 Architecture and vertebral fracture. *Calcif Tissue Int* **53**(Suppl 1):S139–S142.
- Legrand E, Chappard D, Pascaretti C, Duquenne M, Krebs S, Rohmer V, Basle MF, Audran M 2000 Trabecular bone microarchitecture, bone mineral density and vertebral fractures in male osteoporosis. *J Bone Miner Res* **15**:13–19.
- Gordon CL, Webber CE, Adachi JD, Christoforou N 1996 *In vivo* assessment of trabecular bone structure at the distal radius from high-resolution computed tomography images. *Phys Med Biol* **41**:495–508.
- Laib A, Hildebrand T, Hauselmann HJ, Ruegsegger P 1997 Ridge number density: A new parameter for *in vivo* bone structure analysis. *Bone* **21**:541–546.
- Laib A, Hauselmann HJ, Ruegsegger P 1998 *In vivo* high resolution 3D-QCT of the human forearm. *Technol Health Care* **6**:329–337.
- Majumdar S, Genant HK, Grampp S, Newitt DC, Truong V-H, Lin JC, Mathur A 1997 Correlation of trabecular bone structure with age, bone, mineral density, and osteoporotic status: *In vivo* studies in the distal radius using high-resolution magnetic resonance imaging. *J Bone Miner Res* **12**:111–118.
- Gordon CL, Webber CE, Christoforou N, Nahmias C 1997 *In vivo* assessment of trabecular bone structure at the distal radius from high-resolution magnetic resonance images. *Med Phys* **24**:585–593.
- Link TM, Majumdar S, Augat P, Lin JC, Newitt D, Lu Y, Lane NE, Genant HK 1998 *In vivo* high resolution MRI of the calcaneus: Differences in trabecular structure in osteoporosis patients. *J Bone Miner Res* **13**:1175–1182.
- Majumdar S, Kothari M, Augat P, Newitt DC, Link TM, Lin JC, Lang T, Lu Y, Genant HK 1998 High-resolution magnetic resonance imaging: Three-dimensional trabecular bone architecture and biomechanical properties. *Bone* **22**:445–454.
- Wehrli FW, Hwang SN, Ma J, Song HK, Ford JC, Haddad JG 1998 Cancellous bone volume and structure in the forearm: Noninvasive assessment with MR microimaging and image processing. *Radiology* **206**:347–357.
- Ma J, Wehrli FW, Song HK 1996 Fast 3D large-angle spin-echo imaging (3D FLASE). *Magn Reson Med* **35**:903–910.
- Song HK, Wehrli FW 1999 *In vivo* micro-imaging using alternating navigator echoes with applications to cancellous bone structural analysis. *Magn Reson Med* **41**:947–953.
- Hwang SN, Wehrli FW 1999 Estimating voxel volume fractions of trabecular bone on the basis of magnetic resonance images acquired *in vivo*. *Int J Imaging Syst Technol* **10**:186–198.
- Saha PK, Gomberg BR, Wehrli FW 2000 Three-dimensional digital topological characterization of cancellous bone architecture. *Int J Imaging Syst Technol* **11**:81–90.
- Gomberg BG, Saha PK, Song HK, Hwang SN, Wehrli FW 2000 Application of topological analysis to magnetic resonance images of human trabecular bone. *IEEE Trans Med Imaging* **19**:166–174.
- Hwang SN, Wehrli FW 2000 Subvoxel processing: A new method for alleviating partial volume blurring in MR images of trabecular bone. *Proc Int Soc Magnetic Resonance in Medicine, 8th Int Meeting, Int Soc Magnetic Resonance in Medicine, Denver, CO, USA*, pp. 2134.
- Nelson DA, Kleerekoper M 1996 What is a vertebral fracture? In: Marcus R, Feldman D, Kelsey J (eds.) *Osteoporosis*. Academic Press, San Diego, CA, USA, pp. 613–621.
- O'Neill TW, Silman AJ 1997 Definition and diagnosis of vertebral fracture. *J Rheumatol* **24**:1208–1211.
- Wehrli FW, Hopkins JA, Hwang SN, Song HK, Snyder PJ, Haddad JG 2000 Cross-sectional study of osteopenia by quantitative magnetic resonance and bone densitometry. *Radiology* **217**:527–538.
- Eastell R, Cedel SL, Wahner HW, Riggs BL, Melton LJ III 1991 Classification of vertebral fractures. *J Bone Miner Res* **6**:207–215.
- Steiner E, Jergas M, Genant HK 1996 *Radiology of osteoporosis*. In: Marcus R, Feldman D, Kelsey J (eds.) *Osteoporosis*. Academic Press, San Diego, CA, USA, pp. 1019–1050.
- Parfitt AM 1992 Implications of architecture for the pathogenesis and prevention of vertebral fracture. *Bone* **13**:S41–S47.
- Feldkamp LA, Goldstein SA, Parfitt AM, Jesion G, Kleerekoper M 1989 The direct examination of three-dimensional bone architecture *in vitro* by computed tomography. *J Bone Miner Res* **4**:3–11.
- Lane NE, Haupt D, Kimmel DB, Modin G, Kinney JH 1999 Early estrogen replacement therapy reverses the rapid loss of trabecular bone volume and prevents further deterioration of connectivity in the rat. *J Bone Miner Res* **14**:206–214.
- Pothuau L, Porion P, Lespessailles E, Benhamou CL, Levitz P 2000 A new method for three-dimensional skeleton graph analysis of porous media: Application to trabecular bone microarchitecture. *J Microsc* **199**(Pt 2):149–161.
- Kinney JH, Ladd AJC 1998 The relationship between three-dimensional connectivity and the elastic properties of trabecular bone. *J Bone Miner Res* **13**:839–845.

34. Hahn M, Vogel M, Pompesius-Kempa M, Delling G 1992 Trabecular bone pattern factor—a new parameter for simple quantification of bone microarchitecture. *Bone* **13**:327–330.
35. Hildebrand T, Rüegsegger P 1997 Quantification of bone microarchitecture with the structure model index. *Comput Methods Biomech Biomed Eng* **1**:15–23.
36. Hildebrand T, Laib A, Muller R, Dequeker J, Ruegsegger P 1999 Direct three-dimensional morphometric analysis of human cancellous bone: Microstructural data from spine, femur, iliac crest, and calcaneus. *J Bone Miner Res* **14**:1167–1174.
37. Aaron JE, Johnson DR, Paxton S, Kanis JA 1989 Secondary osteoporosis and the microanatomy of trabecular bone. *Clin Rheumatol* **8**:84–88.
38. Vesterby A, Mosekilde L, Gundersen HJG, Melsen F, Mosekilde L, Holme K, Sorensen S 1991 Biologically meaningful determinants of the in vitro strength of lumbar vertebrae. *Bone* **12**:219–224.
39. Durand EP, Rüegsegger P 1991 Cancellous bone structure: Analysis of high-resolution CT images with the run-length method. *J Comput Assist Tomogr* **15**:133–139.
40. Gordon CL, Lang TF, Augat P, Genant HK 1998 Image-based assessment of spinal trabecular bone structure from high-resolution CT images. *Osteoporos Int* **8**:317–325.
41. Mosekilde L 1990 Consequences of the remodelling process for vertebral trabecular bone structure: A scanning electron microscopy study (uncoupling of unloaded structures). *Bone Miner* **10**:13–35.

Address reprint requests to:

Felix W. Wehrli, Ph.D.

Department of Radiology

University of Pennsylvania Medical Center

3400 Spruce Street

1 Founders

Philadelphia, PA 19104, USA

Received in original form August 14, 2000; in revised form December 14, 2000; accepted February 6, 2001.